

Direct Synthesis of Carbon Sheathed Tungsten Oxide Nanoparticles via Self-Assembly Route for High Performance Electrochemical Charge Storage Electrode

Yuanyuan Zhou¹, Ilbok Lee², Daeun Kim², Seunghee Han², Jae-Kwang Kim², Donghyun Lee², Song Won Ko³, Sung Gyu Pyo², Hyungbin Son^{2,*}, and Songhun Yoon^{2,*}

¹*School of Engineering, Brown University, Providence, RI 02912, United States*

²*School of Integrative Engineering, Chung-Ang University, 221, Heukseok-Dong, Dongjak-Gu, Seoul 156-756, Republic of Korea*

³*Materials Research Institute, Pennsylvania State University, University Park, PA 16802 United States*

Using a stabilizing agent-assisted co-assembly method, a novel nanocomposite of mesoporous carbon embedded with uniform tungsten oxide nanorods is obtained, which is converted into carbon-sheathed tungsten oxide nanoparticles by delicate calcination and further reduction. Through optimization of tungsten content, it is found that highly crystalline tungsten oxide nanoparticles are uniformly coated with an ultra-thin carbon layer. When applied into electrochemical charge-storage electrodes for supercapacitor and lithium-ion battery, an excellent average capacitance (129 F g⁻¹, above 400 F cm⁻³), higher rate performance and significantly advanced cycle stability are observed. These improved charge storage properties are attributed to improved electrical conductivity and enhanced structural stability, which is induced by uniform carbon coating on partially reduced tungsten oxide nanoparticles.

Keywords: Carbon Sheathed Tungsten Oxide, Self-Assembly, Nanoparticles, Supercapacitor Electrode, Anode in Lithium Ion Battery.

1. INTRODUCTION

As the demand for rapid development of portable devices and electrical vehicles increases, electrochemical energy storage devices such as supercapacitors (SCs) and lithium-ion batteries (LIBs) became more prevailing.¹⁻³ Especially, transition metal oxides (such as NiO_x, CoO_x, and MoO_x) are attracting significant attention in the replacement of traditional carbon-based electrodes in SCs and LIBs because of their high capacitance/capacity and relatively low cost.⁴⁻⁷ Among them, nanostructured MoO_x exhibited a significantly improved electrode performance as anode in LIB.² As another novel electrode material, especially, tungsten oxide with a high density of ~7.16 g cm⁻³ have been considered as a promising candidate for a high-volumetric charge-storage electrode.^{8,9} Compared with molybdenum-based electrode material, tungsten oxide is also more inexpensive and safer.^{8,10} However, bulk tungsten trioxide (WO₃) possesses poor

electrical conductivity and long ionic diffusion length during charging process, making it an unsuitable electrode material for SCs and LIBs.^{8,9,11} In this context, bulk tungsten trioxide has to be engineered in order to meet the fast electron and charge transport requirements for practical use. Nano-structuring and carbon coating are recognized as effective approaches to improve the electrode performance of low-conductivity transition metal oxides.^{4,12} Furthermore, tungsten trioxide can be converted into the partially reduced tungsten oxide (WO_{3-x}) phase in a reducing atmosphere, which exhibited a great enhancement of electrical conductivity.^{10,13} As described in our previous reports,^{8,9} ordered mesoporous WO_{3-x} prepared by a hard-template method exhibits 150 F g⁻¹ peak capacitance as a supercapacitor electrode and 748 mAh g⁻¹ capacity as a lithium-ion battery anode, reflecting the effectiveness of nano-structuring and partial reduction of the tungsten oxide-based material.⁸ Another interesting result using mesoporous nanocomposite between tungsten oxide and carbon was reported by our group, where di-block

*Authors to whom correspondence should be addressed.

copolymer was used as structure directing agent.^{14,15} Due to high developed mesoporosity and complete nanocomposite between tungsten oxide and carbon, a significantly improved supercapacitor performance was observed.

As another interesting nanostructure, tungsten oxide nanoparticles have not been widely investigated as charge-storage electrodes.¹² It is well-known that pure metal oxide nanostructures exhibit the disadvantage of facile particle aggregation during the charge-storage process.^{16,17} Furthermore, when compared with conventional single-crystalline or polycrystalline materials, the high contact resistance has been observed in nanostructured metal oxides, which is attributed to poor electron transfer between individual nanoparticles.¹⁸ To overcome these obstacles, thin-layered carbon coating has been recognized as a reasonable solution. In general approach to surface coating, metal oxides were synthesized first, a carbon precursor was added to locate the surface of metal oxide particles, and finally, heat treatment was conducted under an inert atmosphere to produce the carbon-sheathed metal oxide.¹⁹ However, such method is time-consuming and complicated; accordingly, development of a simple one-step synthesis without further coating process is highly desired. Although one-pot approaches based on hydrothermal or solvent-thermal methods have been reported in other transition metal oxides.^{20,21} However, a carbon-sheathed tungsten oxides are hard to be prepared through the reported one-pot route because most tungsten precursors are highly moisture-sensitive. Therefore, the development of a novel and simple method to coat a thin carbon layer onto tungsten oxide nanoparticles is actively sought.

In this work, mesoporous carbon embedded with tungsten nanorods (CW) is prepared first through the one-step co-assembly method. Then, carbon-sheathed tungsten oxide nanoparticles (CSW) and reduced carbon-sheathed WO_{3-x} (RCSW) are obtained by following delicate calcination and final reduction process, respectively. As-prepared materials are fabricated into supercapacitor electrode and lithium ion battery anode. The charge storage properties of CSW and RCSW are investigated using various electrochemical methods.

2. EXPERIMENTAL DETAILS

2.1. Materials Preparation

WO_{3-x} nanorods embedded mesoporous carbon (CW), carbon-sheathed WO_3 (CSW), and WO_{3-x} (RCSW) nanoparticles were prepared as follows. WCl_6 (0.2 g; Aldrich) was dissolved in 5 g of ethanol (EtOH) to form solution A. Citric acid (0.2 g; Aldrich) was dissolved in 5 g of EtOH to form solution B. Solution B was mixed with solution A to form solution C. Pluronic F127 (0.8 g; Mw = 12,600 g mol^{-1} , Aldrich) was dissolved in 8 g of EtOH. After stirring at 40 °C for 2 h, a clear transparent solution was obtained. Solution C was then added dropwise under stirring with sequential slow addition of 2.5 g of

the self-made resol ethanolic solution,⁶ immediately yielding a dark blue solution. After vigorous stirring for 2 h, the transparent solution was poured into a large dish and kept in an ambient environment for 1 d, after which time a glue-like film formed. The as-formed film was then heated at 100 °C for 24 h, resulting in a fragile transparent polymer film. After grinding, the polymeric product was carbonized at 450 °C for 2 h and then at 600 °C for 2 h under a nitrogen atmosphere (the temperature ramping rate was 5 °C min^{-1} up to 450 °C and 2 °C min^{-1} after 450 °C). After cooling down to room temperature, the product was obtained as a black powder and was designated as CW. For preparation of CW materials with lower and higher tungsten concentrations, 0.1 g and 0.4 g of WCl_6 were instead added into the precursor solution above, and the resulting samples were designated as CW-L and CW-H, respectively. The CW sample was transferred to a furnace and calcined in laboratory air at 450 °C for 30 min (the ramping rate was 6 °C min^{-1}). The resulting yellow product was collected and designated as CSW material. The RCSW material was obtained by post-heating the CSW powders in a 5% H_2/N_2 (v/v) atmosphere at 500 °C for 30 min.

2.2. Electrode Fabrication

To prepare a supercapacitor electrode, a mixture of CSW and/or RCSW, polytetrafluoroethylene (PTFE) binder, and carbon black (in a 10:1:1 weight ratio) was dispersed in isopropyl alcohol and coated on a round Ti mesh (1 cm^2) as the current collector. The electrode resistance was negligible when 10 wt% conducting materials were added. The resulting electrode plate was pressed and dried under vacuum at 120 °C for 12 h. Here, Pt flag counter and SCE reference electrodes were used for a three-electrode cell system using 1.0 M H_2SO_4 as electrolyte. A potentiostat (Ivium®) was utilized to conduct cyclic voltammetry (CV) and electrochemical impedance spectroscopy (EIS) experiments. The scan rate was 1 mV s^{-1} in the CV experiments.

To prepare the CSW and RCSW anode, CW material was mixed with carbon black and polyvinylidene difluoride (PVDF) binder in a weight ratio of 8:1:1 and then dispersed in N-methyl-2-pyrrolidone (NMP) and spread onto a Cu foil (apparent area of 1 cm^2), followed by drying at 120 °C for 12 h and roll-pressing. The anode performance was characterized using a half-cell configuration in which a Li foil (Cyprus Co.) was used as the counter and reference electrode with 1.0 M LiPF_6 in 1:1 (v/v) ethylene carbonate (EC)/dimethyl carbonate (DMC) (Technosemi Chem. Co.) as the electrolyte. Galvanostatic charge–discharge testing in a voltage range 2.5–0 V versus Li/Li^+ was conducted at different current densities varying from 0.1 to 5 C (1 C = 300 mAh g^{-1}) on a WBCS-3000 battery cycler (WonATech Co.) at the ambient temperature. The cycle performance for 10 cycles was recorded at 0.1 C.

2.3. Characterization

The external morphology of the carbon was examined using a scanning electron microscope (SEM, Philips XL30S FEG), whereas pore images were obtained using a transmission electron microscope (TEM, TECNAI G2 T-20S). Energy-dispersive X-ray (EDX) analysis was conducted using an EDX analyzer equipped with an SEM instrument. Small-angle X-ray scattering (SAXS) and wide-angle X-ray diffraction (WAXRD) data were obtained with a Rigaku D/Max 2200 V diffractometer equipped with a rotating anode and Cu K_{α} radiation ($\lambda = 0.15406$ nm). X-ray photoelectron spectroscopy (XPS) experiments were carried out under ultra-high vacuum using the AXIS NOVA high-resolution X-ray photoelectron spectrometer (HR-XPS). Nitrogen sorption isotherms were measured with a Micromeritics ASAP 2420 system, and pore-size distributions (PSD) were analyzed using the Barrett-Joyner-Halenda (BJH).

3. RESULTS AND DISCUSSION

The process of carbon-sheathed tungsten oxide nanoparticle formation is schematically shown in Figure 1. In brief, the four components WCl_6 , citric acid, resol, and Pluronic® F127 (working as a tungsten precursor, stabilizing agent, carbon precursor, and surfactant, respectively) were dissolved and mixed in ethanol in a predetermined order. Through ethanol evaporation, polymerization, and carbonization (step S1), a WO_{3-x} nanoparticle embedded mesoporous carbon (CW) composite was prepared in the first step. Upon time-controlled calcination in air (step S2), most of the carbon phase was burnt and WO_{3-x} was oxidized to WO_3 , producing the carbon-sheathed tungsten trioxide nanoparticle (CSW). With further calcination in

a reducing atmosphere, CSW was converted to carbon-sheathed reduced tungsten oxide nanoparticles (RCSW) by oxygen removal from the crystal structure of tungsten trioxide by hydrogen gas.¹⁰

Citric acid was found to play a key role in the successful preparation of carbon-sheath tungsten oxide nanoparticles (CSW and RCSW); in the absence of citric acid, the resol/F127/ WCl_6 solution would otherwise be unstable in the ambient environment and rapidly yield a precipitate during stirring. Similar to our previous research about tri-constituent co-assembly between resols, titanium citrate complex, and F127, it is reasonably deduced that complexation between tungsten precursors and citric acid leads to protection tungsten ions from interaction with the resols and F127.^{22,23} This molecular level stability was evidenced by the transparency of the solution. After solvent evaporation/heat treatment, high temperature carbonization was conducted. Because of the hydrogen-bonding based strong interaction between tungsten precursor and surfactant/polymer, the oxidation and crystal growth of the tungsten-containing phase is severely retarded even at 600 °C;¹⁶ as a result, unique composite structure as shown in Figure 2 was observed, where isolated reduced tungsten oxide (WO_{3-x}) nanorods were embedded within mesoporous carbon matrix. Here, observed pores were attributed to thermal decomposition of the F127 surfactant, which has been frequently reported. One can expect that the homogeneous isolation of tungsten oxide nanorods by uniform pores in CW can be beneficial for maintaining nanorod morphology and homogeneous carbon

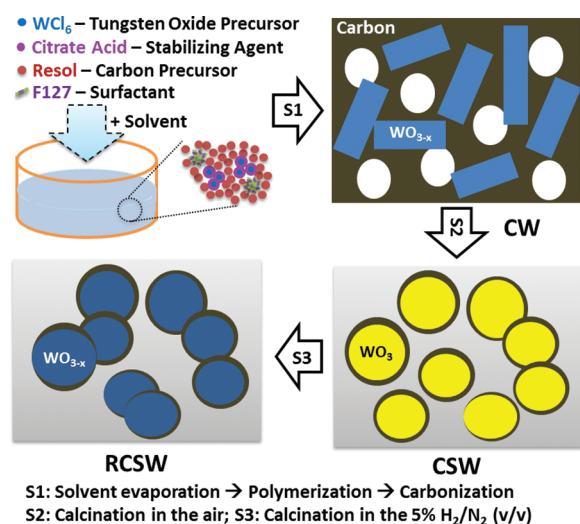


Figure 1. Schematic representation of direct synthesis of carbon-sheathed WO_3 and WO_{3-x} nanoparticles converted from WO_{3-x} nanorods @ mesoporous carbon.

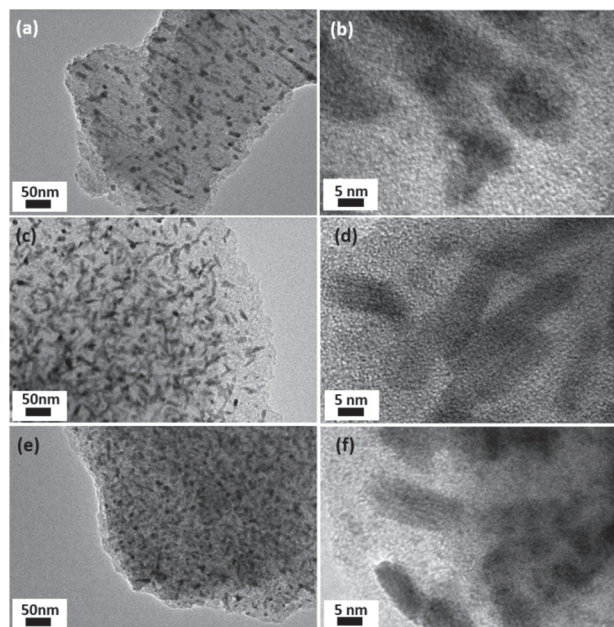


Figure 2. TEM images of WO_{3-x} nanorod @ mesoporous carbon (CW series), CW-L (a, b), CW (c, d), and CW-H (e, f) showing the morphology change of CW materials according to the amount of tungsten precursor added.

coating in CSW due to facile oxygen supply and prohibition of nanoparticle aggregation. The effect of the amount of added tungsten precursor on the morphology of the CW materials was next studied; Figure 2 shows TEM morphologies of a series of CW materials with varying amounts of added tungsten precursor. For all composite samples (CW-L, CW, and CW-H), WO_{3-x} exhibited a nanorod crystalline morphology, while the carbon matrix was of an amorphous nature with mesopores. The high-contrast crystalline WO_{3-x} phase became more populated and their particles became more aggregated with an increase in added tungsten precursor amounts. Hence, it is obvious that in the CW sample, the WO_{3-x} particles have the good size-uniformity and a more regular morphology, indicative of an optimized precursor condition for nanoparticle preparation. In addition, ordering of pore channel was gradually collapsed according to increase of tungsten oxide. In our investigation, note that more developed nanorods of tungsten oxide are more desirable because carbon-sheathed tungsten oxide nanoparticles are of our interest. As described, a mesoporous tungsten oxide-carbon composite was successfully prepared and a significant advance in supercapacitor performance was already reported.¹⁵ Hence, CW was selected for preparation of carbon-sheathed tungsten oxide nanoparticle preparation.

The nitrogen sorption isotherms of CW-L, CW, and CW-H are shown in Figure 3(a). CW-L, CW, and CW-H all showed a typical mesoporous behavior with a hysteresis loop from $P/P_0 = 0.4-0.6$, reflective of a narrow pore-size distribution. The sorption volumes ($582 \text{ m}^2 \text{ g}^{-1}$ for CW-L, $374 \text{ m}^2 \text{ g}^{-1}$ for CW, $292 \text{ m}^2 \text{ g}^{-1}$ for CW-H) and BET surface areas ($0.40 \text{ cm}^3 \text{ g}^{-1}$ for CW-L, $0.18 \text{ cm}^3 \text{ g}^{-1}$ for CW, $0.14 \text{ cm}^3 \text{ g}^{-1}$ for CW-H) were decreased with larger amounts of added tungsten precursor. According to the BJH pore-size distribution based on the desorption branch of the isotherms in Figure 3(b), a nearly identical pore size peak at $\sim 3.5 \text{ nm}$ was shown to be monodisperse, which can be attributed to the same pore-forming mechanism by F127 surfactant;^{7,24} as the added amount of tungsten precursor is increased, the pore-size distribution becomes broadened, which is in good agreement with the collapse in pore structure observed in the TEM study. The pore structure was further studied by SAXS (Fig. 3(c)). CW-L showed a dominant peak at $2\theta = \sim 1.1^\circ$, indicative of the higher ordering of the pore channel arrays with a lattice parameter of $\sim 9 \text{ nm}$ (P6mm space group).⁷ CW also showed a slight shoulder peak, while no peak was observed for CW-H. The vanishing peak in the SAXS result is highly consistent with the broadening of pore-size distribution and direct TEM observation of pore structure collapse. From above preparation, composites of the CW series have been shown to be successfully prepared through tri-constituent co-assembly of a tungsten precursor, resols, and F127 with the assistance

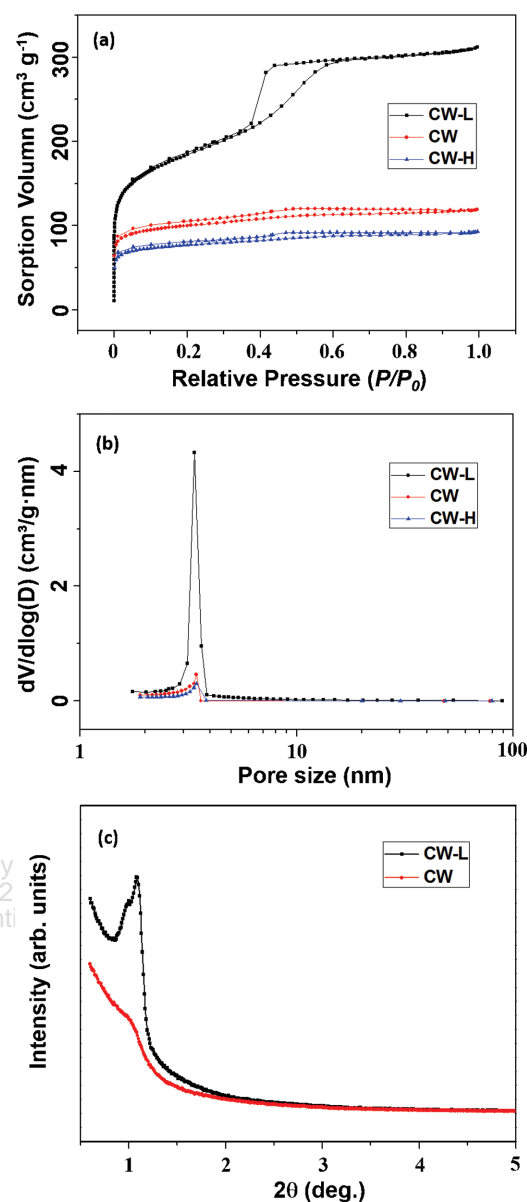


Figure 3. (a) Nitrogen sorption isotherms of CW-L, CW, and CW-H samples; (b) calculated pore-size distribution using the BJH method for CW-L, CW, and CW-H samples; (c) SAXS patterns for CW-L and CW. SAXS pattern for CW-H was not shown here because of the absence of observed scattering peaks.

of citric acid stabilization. In order to obtain high-quality carbon-sheathed tungsten oxide nanoparticles (CSW and RCSW), the CW material with highly dispersed WO_3 nanorods was selected to conduct the following conversion into CSW and RCSW.

Figure 4 presents X-ray diffraction patterns of CW, CSW, and RCSW samples. The corresponding main oxide phases could be clearly assigned to $\text{W}_{32}\text{O}_{84}$ (JCDs PDF #01-077-0810), WO_3 (JCDs PDF #00-020-1324), and $\text{WO}_{2.83}$ (JCDs PDF #00-036-0103) in CW, CSW, and RCSW, respectively. The inset sample pictures visualize the color change upon conversion (black for CW,

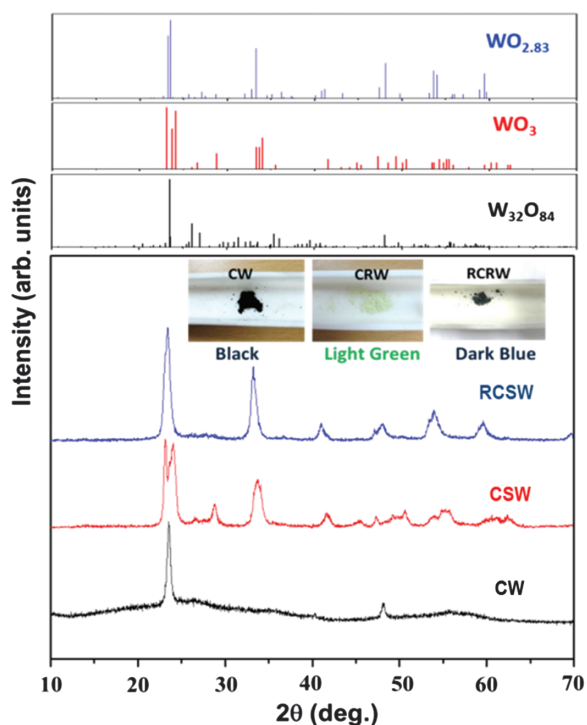


Figure 4. X-ray diffraction patterns of CW, CSW, and RCSW (inset pictures show the sample color).

light green for CSW, and dark blue for RCSW), directly indicative of a phase transformation upon heat treatment.¹² As expected, an amorphous carbon background disappeared after burning process, implying that most of the carbon phase was burnt during the S2 process. Regardless of high-temperature calcination (S2 and S3), the obvious peak broadening in CSW and RCSW patterns could be seen, indicating that the oxide phase in the as-prepared CSW and RCSW samples is present on the nanoscale. The average oxidation state of the present tungsten oxide phase was calculated based on the stoichiometry of the phase formula, which yielded a value of +5.25, +6, and +5.66 for CW, CSW, and RCSW, respectively. In order to further study oxidation-state change, high-resolution XPS spectra were acquired for W_{4f} in each sample as shown in Figure 5. CSW showed a typical well-resolved peak doublet at 35.3 and 37.4 eV, indicative of stoichiometric WO_3 with little defects.^{25, 26}

Compared with CSW, the XPS spectra for CW and RCSW showed blue shifts, which verified the reduced states of mixed oxidation state (+6 and less) is expected in both CW and RCSW samples, the acquired spectra did not show an obvious mixture of W^{6+} or less. Instead, predominant peaks at 34.5 and 36.8 eV were observed, corresponding to an oxidation state of W^{5+} .^{25, 26} This result demonstrated that the tungsten species on the surface of the tungsten oxide phase in CW and RCSW is mostly W^{5+} . In RCSW, a complete coverage by W^{5+} species on the surface was certainly due to carbon-sheathing effect, which

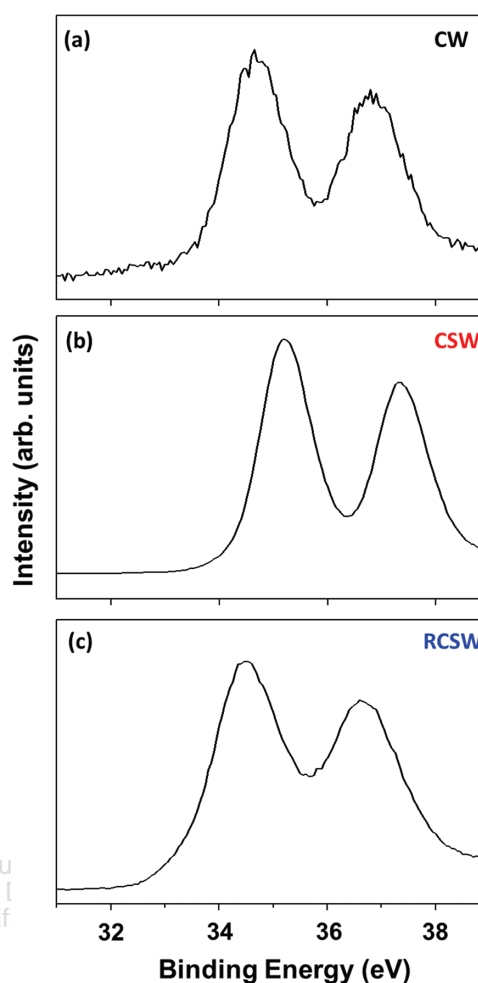


Figure 5. XPS spectra for W_{4f} in (a) CW, (b) CSW, and (c) RCSW samples.

can maintain surface reduction state even after air exposure of tungsten oxide nanoparticles with high contact area. Furthermore, a higher electrical conductivity is expected than bulk WO_3 material.²⁵

The crystallographic and external morphologies of CSW and RCSW using TEM are shown in Figures 6(a–d). As expected, CSW was composed of interconnected nanoparticles with a uniform size of ~ 20 nm. Upon conversion, unavoidable particle aggregation happened in CW, which results in the growth of nanoparticles in RCSW as shown in Figure 6(f). However, it is certain that high temperature heat treatment of CSW in a reductive atmosphere did not cause serious crystal coarsening, which is likely due to the effective isolation of the tungsten oxide particles by the carbon coating in CSW. From Figures 6(b and d), it was revealed that an amorphous carbon layer exists as thin as 1–2 nm, which is closely attached to highly crystalline WO_3 and/or WO_{3-x} particles, respectively. The as-appeared crystal fringes with interspacings of 0.385 nm in Figure 5(b) and 0.376 nm in Figure 5(e) which could be

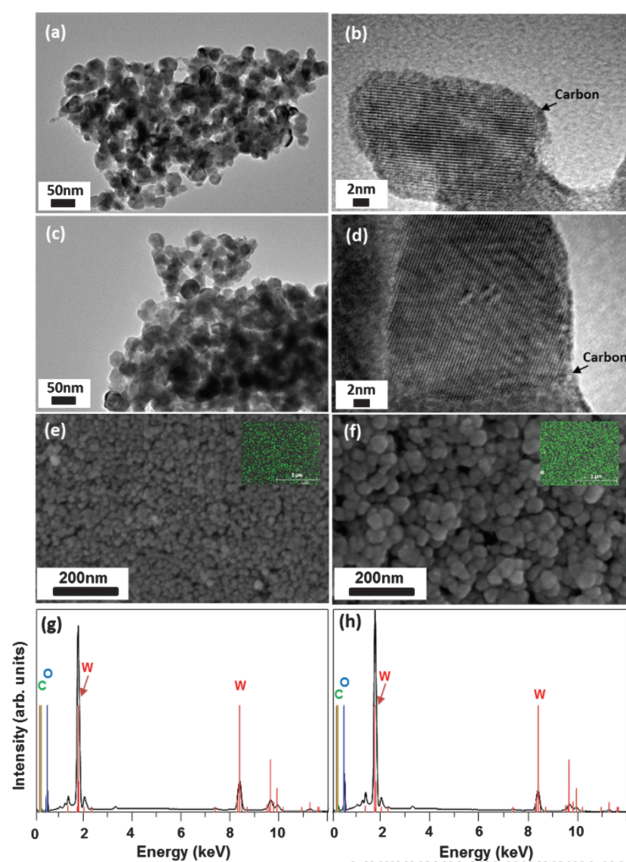


Figure 6. (a, b) TEM images of CSW; (c, d) TEM images of RCSW; (e) SEM image of CSW, inset is the carbon elemental mapping; (f) SEM image of RCSW, inset is the carbon elemental mapping; (g) EDS spectrum for CSW; (h) EDS spectrum for RCSW.

assigned to the (001) and (010) plane of the orthorhombic WO_3 and monoclinic $\text{WO}_{2.83}$ crystal, respectively, which is in agreement with XRD results. It is worth mentioning that the ultra-thin carbon layer could be transparent, which explains why the apparent colors of CSW and RCSW are yellow and blue, respectively, while carbon-coated metal oxides prepared by other methods are mostly black.^{12, 21} The retention of color is an implication of the possible fabrication of electrochromic electrodes consisting of CSW and RCSW, which is one of the most significant applications of tungsten oxide-based materials.²⁵

Figures 6(e–f) shows the SEM images of the CSW and RCSW samples, which were examined in order to verify their interconnected nanoparticle morphologies. For CSW, a typical external morphology of stacked nanoparticles was present with an estimated particle size of 20 nm, similar to the crystal size estimated from the TEM image in Figure 6(a), indicating that the particles in the SEM image are single-crystalline. However, for RCSW, apparent increase of particle sizes was observed, suggesting that at least a couple of nanoparticles aggregate during the reductive conversion. Nevertheless, the invariant crystal size from TEM analysis (Figs. 6(b and d)) exhibited that

the crystal coarsening is greatly hindered. This is probably associated with preventing thin carbon layer on the particle surface in CSW. The insets in Figures 6(e and f) display the carbon elemental mapping on the CSW and RCSW sample, showing a uniform carbon phase coating, while the EDS spectra (Figs. 6(g and h)) indicate the presence of a minor amount (<3%) of carbon phase in the CSW and RCSW samples. This uniform but thin conductive carbon is expected to enhance the electrical conductivity of prepared material, while keeping the beneficial effect of tungsten oxide nanoparticles when applied into charge storage electrodes.

First, the prepared CSW and RCSW materials were utilized as SC electrodes. Figure 7 displays the

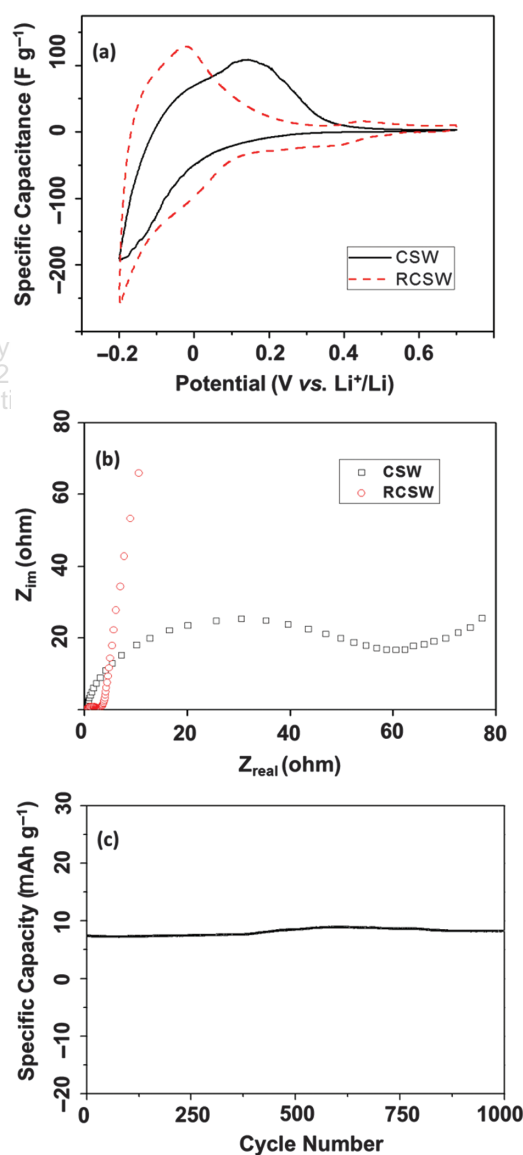
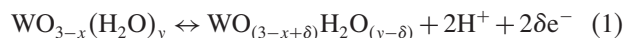


Figure 7. CV curves of (a) CSW and RCSW supercapacitor electrodes at 1 mV s^{-1} ; (b) EIS spectra of CSW and RCSW electrodes; (c) cycle stability of RCSW electrode.

electrochemical properties of CSW and RCSW as SC electrodes. Tungsten oxide has been reported to exhibit pseudocapacitive charging behavior induced by a change in tungsten oxidation state near 0 V versus SCE. This ionic charge phenomenon can be described using Eq. (1);¹³



In this process, the oxidation state of tungsten oxide is converted from +5 to +6, reversibly.¹⁴ As shown in Figure 7(a), typical redox peak pairs were clearly observed for both electrodes, which is associated with the pseudocapacitive reaction of tungsten oxide described in Eq. (1). About CSW electrode, the specific peak capacitance (C_{sp}) in the anodic scan was as high as 108.5 F g^{-1} , even comparable to the metallic mesoporous WO_{3-x} electrode (109 F g^{-1}) prepared using a complicated hard-templating method.¹³ When considering much less porous nature of CSW than ordered mesoporous WO_{3-x} , this high C_{sp} of CSW indicated that nanoparticulate morphology produced a higher SC nature than mesoporous structure. Furthermore, a very high volumetric capacitance of above 400 F cm^{-3} is expected to be obtained from the CSW electrode because of the intrinsically high material density of tungsten oxide ($\sim 7.6 \text{ g cm}^{-3}$).⁸

Compared with CSW, a large increase of C_{sp} was also observed in RCSW electrode (129 F g^{-1}). Furthermore, a polarization resistance associated with the difference in anodic and cathodic peak currents was significantly reduced in RCSW electrode; the dominant symmetrical redox peak pair was shown at ca. -0.05 V versus SCE, and a minor redox peak pair appeared 0.45 V versus SCE.¹ On the contrary, only a broad anodic pseudocapacitive peak at 0.2 V versus SCE was observed for CSW, which is similar to the reported mesoporous WO_{3-x} electrode. This indicated that our RCSW electrode displayed a highly improved rate capability than CSW and m- WO_{3-x} .^{6,9} As displayed in Figure S2, the CV curve shape was mostly retained upon increasing the scan rate; however, the peak capacitance of CSW was reduced to a much smaller value of 6.1 F g^{-1} at 20 mV s^{-1} , indicating that the rate performance is largely enhanced after reduction.

To further understand the performance difference, EIS was performed; the spectra of both electrodes are shown in Figure 7(b). In high frequency region, commonly, both electrode showed semi-circles, indicating that the electrode processes are controlled by electron conduction within electrode and the proton adsorption/desorption electrode surface.¹⁵ Note that RCSW electrode exhibited a greatly reduced semi-circle resistance, which indicated that electrical conduction and pseudocapacitive reaction rate were greatly improved. In the low frequency region, where the electrode reaction process is controlled by electrolyte diffusion, RCSW showed steeper slope, reflecting faster electrolyte transport;¹ the decreased resistance may be also associated with the closer crystal attachment after the S3

process. In Figure 7(c), the long-term cycle performance of the RCSW electrode was evaluated because of its better overall performance; a very stable cycle performance was observed, which can be ascribed to the formation of a stable nanostructure in the RCSW material and a higher resistance to the strong acid electrolyte because of carbon shell formation on the tungsten oxide particles. For comparison, it was reported that a mesoporous tungsten oxide material without a protective carbon coating still showed performance decay during cycling.¹³ Figure 8 shows the anode performance of CSW and RCSW electrodes in lithium-ion batteries. The lithium uptake mechanism of the tungsten

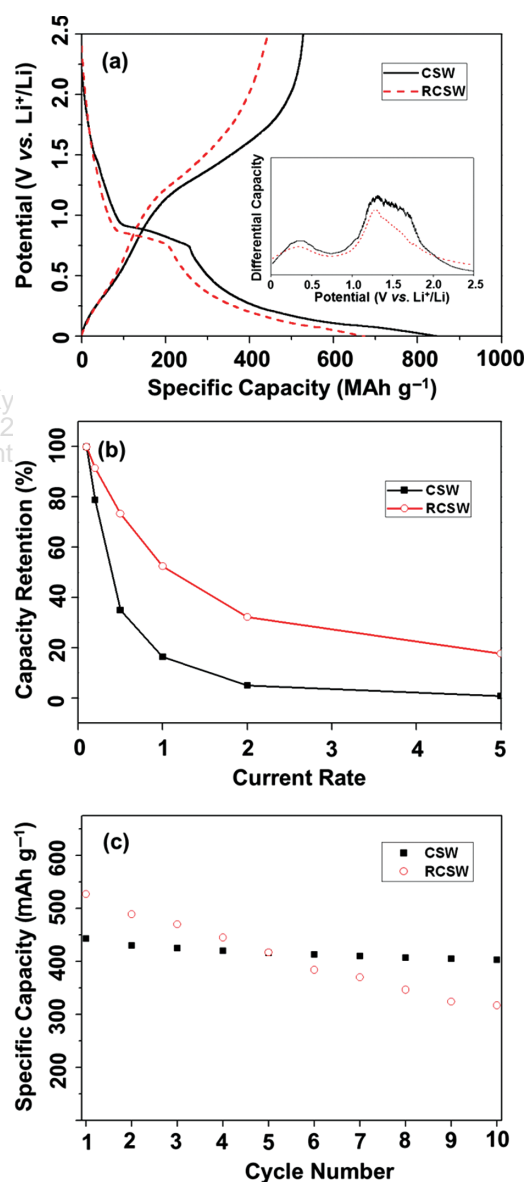
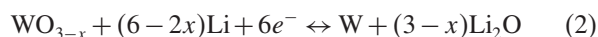


Figure 8. (a) Initial charge–discharge profiles of CSW and RCSW anodes with an inset showing differential capacity plots based on the discharge branches of CSW and RCSW anodes; (b) rate performance and (c) cycle performance of CSW and RCSW anodes.

oxide-based anode is based on the conversion reaction as shown in Eq. (2):⁸



According to the above equation, the capacity of RCSW with $\text{WO}_{2.82}$ as the major phase is reasonably lower than CSW with WO_3 because of the lower oxidation state of the tungsten oxide. The theoretical capacity values of $\text{WO}_{2.83}$ and WO_3 were about ~ 654 and ~ 693 mAh g^{-1} , respectively. From Figure 8(a), the reversible capacity of CSW and RCSW after nanostructuration. The inset figure in Figure 8(a) shows the plots of differential capacity per voltage derived from the discharge branch. The peaks in the inset figure correspond to the plateau in the discharge profile. Two similar peaks at ~ 0.35 and ~ 1.32 V were observed for both CSW and RCSW electrodes, which is also consistent with that found for the reported tungsten oxide-based anode.⁸ However, the RCSW showed a relatively less intense peak at ~ 1.35 V, which can be attributed to the relative lower final oxidation state after discharge. With regard to the initial coulomb efficiency (IE), values of 62% and 66% were calculated from the charge–discharge profiles for CSW and RCSW samples, respectively, in which the parameters for both CSW and RCSW exhibited a much superior performance to that of the state-of-the-art tungsten oxide-based anode (mesoporous reduced tungsten oxide).⁴ Probably, the higher IE in RCSW is mostly due to decreased surface area induced by more aggregation during reduction. However, it is certain that the favorable characteristics such as better conductivity and a more stable composite structure can result in higher IE.^{7,18}

The rate performances of both electrodes were further compared. As shown in Figure 8(b), RCSW retained a discharge capacity of $\sim 17\%$ at a high rate of 2 C, while the capacity of CSW was seriously decayed (2%). Probably, the partially oxidized carbon layer of a few nm is insufficient to provide enough electric percolation networks in CSW, which resulted in low rate capability. Finally, the cycle performances of both electrodes were evaluated. Interestingly, while the cycle performance still remained unsatisfactory for CSW sample (60% capacity retention upon 10 cycles), the RCSW electrode showed a significantly enhanced stable performance (91%) at 10 cycles. This indicated that the weak carbon layer in CSW cannot provide enough mechanical strength to resist high volumetric change during charge–discharge. In the literatures, the cycle performance of tungsten oxide anode was as low as above 20% capacity loss even in the ordered mesoporous WO_{3-x} anode.⁸ To our knowledge, hence, RCSW anode exhibited one of the best cycle stability. In this material, homogeneously coated with rigid carbon layer certainly reduces the aggregation during conversion reaction with Li^+ , which may result in a significant increase of cycle performance.

4. CONCLUSIONS

In this work, a novel method is described for the preparation of carbon-sheathed tungsten oxide (WO_3 and WO_{3-x}) nanoparticles based on a composite of uniform WO_{3-x} nanorods @ mesoporous carbon. The preparation of WO_{3-x} nanorods embedded mesoporous carbon, as the essential intermediate product, is also optimized. In terms of the electrochemical charge-storage properties of the nanoparticles as a supercapacitor electrode and LIB anode, carbon-sheathed WO_3 has shown an excellent charge-storage capability owing to the conductive carbon coating, while carbon-sheathed WO_{3-x} has exhibited even better performances in rate capability and stability, which is mostly associated with the intrinsic superior electric conductivity of the partially reduced tungsten oxide phase.

Acknowledgments: This work is supported by the National Research Foundation of Korea (NRF) grant funded by the Korea government (MSIP) (No. 2015R1A2A2A03005789). This work is supported by the Chung-Ang University Research Scholarship Grant 2015.

References and Notes

- B. E. Conway, *Electrochemical Supercapacitors*, Kluwer Academic/Plenum Publisher, New York (1999).
- P. Simon and Y. Gogotsi, *Nat. Mater.* 7, 845 (2008).
- J.-M. Tarascon and M. Armand, *Nature* 414, 359 (2001).
- P. Poizot, S. Laruelle, S. Grugeon, L. Dupont, and J.-M. Tarascon, *Nature* 407, 496 (2000).
- M. V. Reddy, G. V. Suba Rao, and B. V. R. Chowdari, *Chem. Rev.* 113, 5364 (2013).
- Y. Zhou, Y. Kim, C. Jo, J. Lee, C. W. Lee, and S. Yoon, *Chem. Comm.* 47, 4944 (2011).
- Y. Zhou, C. W. Lee, S.-K. Kim, and S. Yoon, *ECS Electrochem. Lett.* 1, A17 (2012).
- S. Yoon, C. Jo, S. Y. Noh, C. W. Lee, J. H. Song, and J. Lee, *Phys. Chem. Chem. Phys.* 13, 11060 (2011).
- S. Yoon, E. Kang, J. K. Kim, C. W. Lee, and J. Lee, *Chem. Comm.* 47, 1021 (2011).
- G.-A. Nazri and G. Pisoia, *Lithium Batteries: Science and Technology*, Springer, Boston (2009).
- A. R. West, *Basic Solid State Chemistry*, Second edn., John Wiley & Sons Inc., Singapore/Toronto/New York (1999).
- W.-M. Zhang, X.-L. Wu, J.-S. Hu, Y.-G. Guo, and L.-J. Wan, *Adv. Funct. Mater.* 18, 3941 (2008).
- E. Kang, S. An, S. Yoon, J. K. Kim, and J. Lee, *J. Mater. Chem.* 20, 7416 (2010).
- C. Jo, I. Hwang, J. Lee, C. W. Lee, and S. Yoon, *J. Phys. Chem. C* 115, 11880 (2011).
- C. Jo, J. Hwang, H. Song, A. H. Dao, Y.-T. Kim, S. H. Lee, S. W. Hong, S. Yoon, and J. Lee, *Adv. Funct. Mater.* 23, 3747 (2013).
- H. Liu, L. J. Fu, H. P. Zhang, J. Gao, C. Li, Y. P. Wu, and H. Q. Wu, *Electrochem. Solid-State Lett.* 9, A529 (2006).
- Y. Wang, H. J. Zhang, L. Lu, L. P. Stubbs, C. C. Wong, and J. Lin, *ACS Nano* 4, 4753 (2010).
- Y. Zhou and S. Yoon, *Electrochem. Commun.* 40, 54 (2014).
- M. G. Choi, Y.-G. Lee, S.-W. Song, and K. M. Kim, *J. Power Sources* 195, 8289 (2010).
- Z. Wang, J. S. Chen, T. Zhu, S. Madhavi, and X. W. Lou, *Chem. Commun.* 46, 6906 (2010).

21. H. R. Lee, H. J. Kim, J. H. Park, and D. H. Yoon, *J. Nanosci. Nanotechnol.* 13, 4141 (2013).
22. Y. Zhou, J. Lee, C. W. Lee, M. Wu, and S. Yoon, *Chem. Sus. Chem.* 5, 2376 (2012).
23. J. J. Cruywagen, L. Krüger, and E. A. Rohwer, *J. Chem. Soc. Dalton Trans.* 1727 (1991).
24. R. Liu, Y. Ren, Y. Shi, F. Zhang, L. Zhang, B. Tu, and D. Zhao, *Chem. Mater.* 20, 1140 (2008).
25. Y. Zhou, S.-H. Ko, C. W. Lee, and S. Yoon, *J. Power Sources* 244, 777 (2013).
26. A. P. Shpak, A. M. Korduban, M. M. Medvedskij, and V. O. Kandyba, *J. Electron Spectrosc. Relat. Phenomena* 172, 156 (2007).
27. S.-H. Lee, R. Deshpande, P. A. Parilla, K. M. Jones, B. To, A. H. Mahan, and A. C. Dillon, *Adv. Mater.* 18, 763 (2006).

Received: 12 September 2015. Accepted: 23 October 2015.

Delivered by Ingenta to: Sung Kyun Kwan University
IP: 115.145.129.113 On: Mon, 12 Dec 2016 06:11:05
Copyright: American Scientific Publishers